Juliette A. Saint, Marca M. Doeff*, and James Wilcox

Chem. Mater.

Electrode Materials with the $Na_{0.44}MnO_2$ Structure: Effect of Titanium Substitution on Physical and Electrochemical Properties

Partial titanium substitution of electrodes with the $Na_{0.44}MnO_2$ structure modifies the voltage characteristics and improves thermal properties. The electrochemical behavior is also sensitive to the synthetic method used to make the materials. Glycine-nitrate combustion results in smaller particles, which increases the rate capabilities of both the Li_xMnO_2 and $Li_xTi_{0.11}Mn_{0.89}O_2$ electrodes.

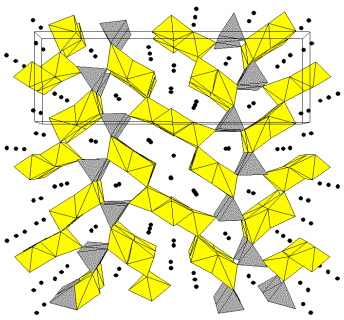

FOR TABLE OF CONTENTS USE ONLY

Electrode Materials with the $Na_{0.44}MnO_2$ Structure: Effect of Titanium Substitution on Physical and Electrochemical Properties

Juliette A. Saint, Marca M. Doeff, and James Wilcox

Materials Sciences Division

Lawrence Berkeley National Laboratory

University of California

Berkeley, CA 94720

Abstract

The physical and electrochemical properties of Li_xMnO_2 and $Li_xTi_{0.11}Mn_{0.89}O_2$ synthesized from precursors made by glycine-nitrate combustion (GNC) and solid-state synthesis methods (SS) are examined in this paper. The highest specific capacities in lithium cells are obtained for SS-Li_xMnO_2 electrodes at low current densities, but GNC-$Li_xTi_{0.11}Mn_{0.89}O_2$ electrodes show the best high rate performance. These results can be explained by changes in the voltage characteristics and differences in the particle morphologies induced by the Ti-substitution and synthesis method. Ti-substitution also results in a decrease in the electronic conductivity, but greatly improves the thermal properties and imparts dissolution resistance to the electrode. For these reasons, it is preferable to use $Li_xTi_{0.11}MnO_{0.89}O_2$ in lithium battery configurations rather than Li_xMnO_2. Suggestions for improving the electrochemical performance of the Ti-substituted variant are given based on the results described herein.

Introduction

Lithium manganese oxide Li_xMnO_2 with the $Na_{0.44}MnO_2$ structure has been extensively investigated as a cathode material for rechargeable lithium batteries.[1, 2, 3, 4] It can be cycled at high rates in lithium/liquid electrolyte cells[1] at room temperature without losses, shows excellent reversibility in lithium/polymer electrolyte cell configurations at 85°C,[4] and appears to be resistant against degradation due to over-charge.[3] The characteristics of robustness and excellent reversibility are particularly attractive when the requirements for hybrid electric vehicle (HEV) are taken into account; cost constraints mandate the use of inexpensive electrodes such as manganese oxides, but materials must demonstrate abuse tolerance and be able to withstand thousands of high power cycles. As with other types of manganese-containing electrodes, however, some dissolution of manganese is observed when

cells are cycled in $LiPF_6$-containing electrolytic solutions at 55°C, causing degradation of the electrode material.[5] For higher energy applications such as plug-in hybrid electric vehicles (PHEVs), the limited specific capacity (~120 mAh/g) achievable in conventional cells is also an issue. The low oxidative stability limit of carbonate-based electrolytes (4.3-4.4 V vs. Li/Li^+) does not allow full extraction of lithium ions from the Li_xMnO_2 structure, so that the full theoretical capacity cannot be cycled. Complete utilization of this electrode material requires development of electrolytes and cell components with improved oxidative stability, so that higher voltage limits may be used without compromising cycle life.

Up to 55% of the manganese in the $Na_{0.44}MnO_2$ structure can be substituted with titanium.[6, 7] Partial substitution appears to impart resistance against dissolution and degradation of the material in electrochemical cells with $LiPF_6$-containing electrolytic solutions at elevated temperature.[5] Saint et al.[8] have also observed a similar protective effect in cells with pyrrolidinium-based ionic liquid electrolytes; Li_xMnO_2 undergoes rapid capacity fading due to an electrochemically induced dissolution/precipitation reaction whereas $Li_xTi_{0.11}Mn_{0.89}O_2$ cycles stably. A possible advantage to the use of pyrrolidinium-based room temperature ionic liquids (RTILs) instead of conventional electrolyte systems composed of organic carbonates and $LiPF_6$ is the greater oxidative stability of the former; e.g., decomposition limits in excess of 5V vs. Li/Li^+ have been observed for lithium bis(trifluoromethanesulfonyl)imide (LiTFSI) dissolved in N-methyl N-propylpyrrolidinium bis(fluorosulfonyl)imide ($P_{13}FSI$) in cyclic voltammetry experiments.[8] In theory, use of RTILs should allow greater utilization of electrode materials with the $Na_{0.44}MnO_2$ structure. However, $Li_xTi_{0.11}Mn_{0.89}O_2$ electrodes exhibited lower capacities initially than Li_xMnO_2 electrodes in the study cited above,[8] where RTIL-containing cells were cycled to 4.4V vs. Li/Li. In contrast, some Ti-substituted materials yielded higher capacities than Li_xMnO_2 in polymer electrolyte cells at elevated temperatures[6] and in devices with conventional

electrolytes charged to 4.8V vs. Li/Li^+.[7] Additionally, materials made with excess lithium salt were observed to have increased capacities under similar conditions.[9] The performance of the titanium-substituted materials is clearly very sensitive to cell configuration, synthesis method, and other factors.

In this paper, we describe work directed towards understanding what properties of Li_xMnO_2 and $Li_xTi_yMn_{1-y}O_2$ compounds are relevant to the differences in electrochemical performances that were observed. An eventual goal is to exploit the high oxidative stability limits of RTILs in order to utilize more fully electrode materials based on the $Na_{0.44}MnO_2$ structure.

Experimental

Synthesis of Li_xMnO_2 and $Li_xTi_{0.11}Mn_{0.89}O_2$

The precursor materials, $Na_{0.44}MnO_2$ and $Na_{0.44}Ti_{0.11}Mn_{0.89}O_2$ were made by a solid-state method (SS) and by glycine-nitrate combustion (GNC). For the solid-state synthesis of $Na_{0.44}MnO_2$, intimately mixed Na_2CO_3 and Mn_2O_3 were heated together at 800°C for 8h. To compensate for a loss of sodium during reaction, an initial excess of Na (Na/Mn≈0.49) was used. X ray powder diffraction patterns were taken to monitor the product for impurities. When Mn_2O_3 was found, an aqueous solution of NaOH in an amount sufficient to react with Mn_2O_3 completely was added and the powder was refired for another 8h. $Na_{0.44}Ti_{0.11}Mn_{0.89}O_2$ was made by heating together well-mixed powders of $Na_2Ti_3O_7$, Mn_2O_3, and Na_2CO_3 in the desired proportions at 850°C for 10h. Chemical analyses performed by Desert Analytics, (Tucson, AZ) on these materials indicated that the Na/T.M ratio (where T.M.= Mn or Mn+Ti) were close to the nominal 0.44 in both cases. These products are designated SS-$Na_{0.44}MnO_2$ and SS- $Na_{0.44}Ti_{0.11}Mn_{0.89}O_2$, respectively, in the text.

Glycine-nitrate combustion synthesis of $Na_{0.44}MnO_2$ was carried out as previously described in reference 1. For the combustion synthesis of $Na_{0.44}Ti_{0.11}Mn_{0.89}O_2$, $TiO(NO_3)_2{\cdot}xH_2O$ was first prepared by hydrolyzing $TiCl_4$ in aqueous ammonia, washing the

product with distilled water to remove chloride ions, and dissolving the oxide in aqueous nitric acid as described in Jung et al.[10] $NaNO_3$ and glycine was then added to the solution, which was then heated until combustion occurred. The product was collected and calcined at 800°C for four hours. The results of the chemical analyses were similar to those obtained on the solid-state products. These products are designated GNC-$Na_{0.44}MnO_2$ and GNC-$Na_{0.44}Ti_{0.11}Mn_{0.89}O_2$ in the text.

$Na_{0.44}MnO_2$ and $Na_{0.44}Ti_{0.11}Mn_{0.89}O_2$ powders were ion exchanged by heating them in a molten salt mixture of 68 mol % $LiNO_3$/ 32 mol % KNO_3 at 230 to 250°C for about 24h. A 5 to 10-fold excess of the lithium salt was used and the process was done three times. Samples were determined to be more than 90% exchanged by XRD and atomic absorption analysis (Desert Analytics, USA). The total alkali metal content (Na +Li) ranged from x=0.28-0.35 in $(Na, Li)_x(Mn, Ti)O_2$ indicating that some oxidation of the products occurred during ion exchange. For the sake of convenience, these products are designated SS- or GNC-Li_xMnO_2 and SS- or GNC-$Li_xTi_{0.11}Mn_{0.89}O_2$ to specify which of the sodium-containing precursors was used in their preparation.

Sample Characterization

The microstructure of the samples was analyzed by scanning electron microscopy/energy dispersive x-ray detection (SEM/EDX) using an environmental scanning electron microscope (S-4300SE/N, Hitachi, Pleasanton, CA).

X-ray diffraction (XRD) powder diffraction was used to assess the phase purity of the products. Patterns were obtained at 300K on a Phillips X'Pert diffractometer equipped with an X'Celerator detector (θ-θ geometry, back monochromator) using Cu K-alpha radiation. Lattice parameters were determined by full pattern matching using the WINPLOTR/Fullprof suite.

Electrochemical Characterization

Composite positive electrodes were prepared by thoroughly mixing the active material (80%) with carbon black (6%), SFG-6 graphite (6%) and polyvinylidene fluoride Kynar^{TM} (8%) in N-methyl-pyrrolidinone and extruding onto carbon coated aluminium foils (Intelicoat Technologies). Electrodes, with loadings between 8 and 15 mg of active material/cm^2, were dried for 24h at room temperature and then for 24h at 100-120°C under vacuum. 2032 coin cells were then assembled in a helium filled dry box (<1ppm H_2O/O_2) using Li metal foils as counter electrodes and Celgard 3401 separators saturated with 1M $LiPF_6$ in 1:2 ethylene carbonate/dimethyl carbonate (EC/DMC, Ferro Corporation). Several coin cells containing each sample were assembled and tested to ensure reproducibility. Lithium insertion/extraction was monitored with a "Mac-Pile" controller (Biologic, S.A., Claix, France) operating in galvanostatic or potentiostatic mode. Cells were charged and discharged at the same rate, unless otherwise noted.

Conductivity measurements

For ac electrical conductivity measurements, approximately 0.5 g of Li_xMnO_2 or $Li_xTi_{0.11}Mn_{0.89}O_2$ powders were initially pressed uniaxially at ~10 kpsi in a 0.5 in. die. The pellets were then transferred into balloon holders and cold isostatically pressed at 200,000 psi. Thin gold electrodes were then sputtered on the two faces of the pellets, using a Bal-Tec SCD 050 sputter coater. AC impedance measurements were carried out on a Solartron Instruments 1260 impedance/gain phase analyzer at selected temperatures. Conductivities were derived from the intercepts of the main capacitative arcs with the z' axes in the Nyquist plots.

Thermal characterization

Differential scanning calorimetry (DSC) experiments were conducted on Li_xMnO_2 and $Li_xTi_{0.11}Mn_{0.89}O_2$ powders electrochemically charged to 4.4V without carbon additives or

binders, and removed from coin cells. The data were acquired at a scan rate of 10°C/min in the temperature range of 30-400°C.

Results and Discussion

$Na_{0.44}MnO_2$ is isostructural with $Na_4Mn_4Ti_5O_{18}$[11] and crystallizes in an orthorhombic lattice (Pbam space group). Figure 1 shows a representation of the structure, looking down the c-axis, and Figure 2a shows the indexed XRD pattern of SS-$Na_{0.44}MnO_2$. (Results of Rietveld refinements have been previously published[4] and are not included here. Discrepancies in peak intensities in Figure 2a are attributable to preferred orientation of the needle-like particles, *vide infra)*. Mn is located in five types of sites: one with square pyramidal coordination by oxygen, and four others having octahedral coordination. Sheets of edge-sharing MnO_6 octahedra and columns of MnO_5 square pyramids share corners to form two types of tunnels. Two sodium sites (labeled Na(1) and Na(2)) in Figure 1) are situated in the large S-shaped tunnels, while another site (Na(3)) is located in the smaller pentagonal tunnels. In the as-prepared material, the sodium sites in the small tunnels are fully occupied while the large-tunnel sites are partially occupied. The main diffusion pathway for sodium ions is along the c-axis, and sodium ions may be either inserted or extracted via chemical or electrochemical processes. Full occupancy of all the sodium sites gives a composition of $Na_{0.66}MnO_2$, close to what is observed at the end of discharge for this material in sodium cells.[12,13] $Na_{0.44}MnO_2$ may also be partially exchanged by solution methods to form compounds with composition $Li_xNa_yMnO_2$ ($x+y \leq 0.44$) [4] or fully ion-exchanged in molten nitrate salts to yield materials with composition Li_xMnO_2 ($x \approx 0.27$-0.35); the exchange process also usually results in partial oxidation. Replacement of sodium with lithium decreases the unit cell volume, which shifts the peaks in the XRD pattern (Figure 2 b).

Li_xMnO_2 can undergo chemical or electrochemical insertion and de-insertion of lithium ions, and may be used as a cathode material in lithium batteries. While it is unlikely that lithium ions occupy the same sites as sodium in this structure, the maximum reversible

composition limit for Li insertion appears to be approximately x=0.66 as with sodium.[1, 2] Insertion past x=0.66 can occur below 2.5V vs. Li/Li^+, but is not completely reversible, and results in eventual capacity losses upon cycling. Based on these observations, the reversible theoretical capacity is 193 mAh/g corresponding to a range of composition of $\Delta x=0.66$.

Partial Ti substitution of Mn in the $Na_{0.44}MnO_2$ structure causes an increase in the unit cell volume[6, 8] which shifts the peaks in the XRD pattern (Figure 2b), but otherwise, the structure is unaffected. The substituted materials undergo similar redox and ion exchange reactions as the parent compound. Based on average bond lengths and site symmetry considerations, it has been shown that Ti^{4+} substitutes for Mn^{4+} in a random fashion in octahedral sites.[6] (In $Na_4Mn_4Ti_5O_{18}$ ($Na_{0.44}Ti_{0.55}Mn_{0.45}O_2$), Ti fully occupies three of the four octahedral Mn sites; the less symmetrical square pyramidal sites still contain Jahn-Teller distorted Mn^{3+}). Because the reversible capacity in this structure is limited by the number of sites for alkali metal ions in the tunnels and only 66% of the Mn in the framework participates in the reversible redox reaction, replacement of up to 34% of the metal should have no adverse impact on the energy density. In fact, Ti substitution lowers the equivalent weight, resulting in modest increases in the theoretical specific capacities (e.g., 198 mAh/g for $Li_xTi_{0.33}Mn_{0.67}O_2$). Interestingly, the capacity obtained between 4.8-2.5V vs. Li/Li^+ for the highly substituted $Li_xTi_{0.55}Mn_{0.45}O_2$ is somewhat greater than predicted if it is assumed that only Mn is electroactive.[7] This indicates that at least some of the Ti^{3+}/Ti^{4+} redox processes occur at higher potentials in this structure than for titanates such as $Li_4Ti_5O_{12}$[14] or anatase,[15] which generally discharge below 2V vs. Li/Li^+. (It is not possible, at present, to determine if Ti is electroactive in compounds that are less highly substituted). In addition, Li_xMnO_2 and its derivatives exhibit the highest potentials for Mn^{3+}/Mn^{4+} redox processes (>4.3V) ever observed for a Li-Mn-O compound,[7] indicating the strong influence of the structure on the electrochemical properties.

The discharge characteristics of lithium cells containing $Na_{0.44}MnO_2$-type tunnel compounds vary as a function of preparation method and Ti substitution. [6] Figure 3 compares differential capacity plots and integrated discharge profiles of lithium cells with electrodes containing Li_xMnO_2 and $Li_xTi_{0.11}Mn_{0.89}O_2$, stepped in 10 mV increments between voltage limits of 2.5 and 4.8V for several cycles. The open circuit potentials for the cells as assembled were about 3.2-3.3V, and all were stepped to 4.8V (i.e., charged) initially. In all cases, the differential capacity plot of the first cycle (dotted line) is somewhat different than the subsequent ones (solid lines), but cycles 2 and 3 are identical to one another. In particular, irreversible capacity above 4.2 V on the first charge is evident and is somewhat greater for the samples made by glycine-nitrate combustion than those made by solid-state methods. The first charge irreversibility is attributable to oxidation of electrolyte and to electrochemically induced decomposition of residual surface species such as Li_2CO_3. [5] The irreversibility decreases on later cycles, but coulombic inefficiencies are still evident in all the cells.

The dQ/dV plots of the Li/Li_xMnO_2 cells (Figures 3a and b) show several well-defined reversible peaks, which are manifested as voltage plateaus in the integrated data. Similar phenomena are observed in stepped potential experiments on $Na/Na_{0.44}MnO_2$ cells,[16] which have been identified as numerous rapid, second order biphasic transitions by in situ XRD experiments. [13] It is likely that these transitions involve site-specific redox processes of the different types of Mn in the structure, which, in turn, are associated with insertion or extraction of alkali metal ions from particular positions in the tunnels. Although these have not been precisely identified, it is probable that the redox processes at lower potentials involve alkali metal ions in the large S-shaped tunnels, whereas those above 4 V involve the higher energy sites in the small pentagonal tunnels.

The dQ/dV plots of the $Li/Li_xTi_{0.11}Mn_{0.89}O_2$ cells (Figures 3c and d) are equally complex, but the peaks are much broader. Because of the random distribution of Ti

throughout the five different transition metal sites, the phase transitions associated with the site-specific redox processes are less sharp.

These transitions are located at somewhat different redox potentials for the four materials (Table 1). Ti-substitution appears to raise the potentials of the biphasic transitions somewhat, particularly those that occur above 4V. A portion of the capacity above 4V is also shifted to higher potentials for both samples made by glycine-nitrate combustion compared to those made by solid-state synthesis, although processes below 3.4V are slightly lowered. The shifting is most dramatic for GNC-$Li_xTi_{0.11}Mn_{0.89}O_2$, which even has some capacity above 4.5V. The reasons for these differences are not entirely clear, but may be attributable to variations in the distribution of Ti in the transition metal framework, and/or the effects of residual sodium in the tunnels. Under the conditions of these slow potentiostatic experiments, the utilization is 70-75% of the theoretical capacity for all the electrodes. The specific capacity varies slightly depending on the cathode material, increasing in the order GNC-$Li_xTi_{0.11}Mn_{0.89}O_2$, SS-$Li_xTi_{0.11}Mn_{0.89}O_2$< GNC-$Li_xMnO_2$< SS-$Li_xMnO_2$.

The tendency for conventional carbonate-based electrolytes to oxidize irreversibly at high potentials vs. Li/Li^+ necessitates lowering the upper voltage limit to 4.4V or below when cycling to assure good capacity retention. Practically, this means that complete extraction of Li ions from the active material structure cannot be achieved, which lowers the utilization. The performance depends not only on the chosen voltage limit, but also on the current density, the choice of active material (Li_xMnO_2 or $Li_xTi_{0.11}Mn_{0.89}O_2$), and how it was made (Figure 4). Below about 1 mA/cm^2, the materials made by solid-state synthesis outperform the analogs made by glycine-nitrate combustion, and both types of unsubstituted materials outperform the $Li_xTi_{0.11}Mn_{0.89}O_2$ samples. The highest specific capacities are obtained with SS-Li_xMnO_2 at low rates and the lowest for GNC-$Li_xTi_{0.11}Mn_{0.89}O_2$. Above 1 mA/cm^2, however, the glycine-nitrate combustion synthesized materials deliver higher specific

capacities than the analogs made by solid-state methods. Surprisingly, GNC-$Li_xTi_{0.11}Mn_{0.89}O_2$ appears to have the best overall rate capability, and SS-$Li_xTi_{0.11}Mn_{0.89}O_2$ the worst.

A somewhat higher capacity is obtained for SS-Li_xMnO_2 than for SS-$Li_xTi_{0.11}Mn_{0.89}O_2$ at every current density, in part reflecting the effect of the shift of some of the capacity to higher potentials (Figure 2 and Table 1), very close to the cutoff voltage used for the experiments summarized in Figure 4. Less Li can be extracted upon charge for SS-$Li_xTi_{0.11}Mn_{0.89}O_2$ than for SS-Li_xMnO_2, which adversely affects its discharge capacity. Modifications of the voltage profile also account for the lower capacities obtained at low current densities for materials made by glycine-nitrate combustion compared to their solid-state synthesized analogs. The poorest performance is that of GNC-$Li_xTi_{0.11}Mn_{0.89}O_2$, which exhibits the most extreme shifting of the voltage profile.

Better results are obtained for the GNC materials at high rates than for the SS analogs; an observation that seems to contradict the paragraph above. This, however, can be explained by particle morphology and size effects. Particles of the $Na_{0.44}MnO_2$ precursor have high aspect ratios (Figure 5a and b) with those made by GNC somewhat shorter on average than ones made by solid-state synthesis. (Note that ion exchange does not affect the physical characteristics of the powders[9]). The needle-like particles of both types of $Na_{0.44}Ti_{0.11}Mn_{0.89}O_2$ are much longer, with most of those made by solid-state synthesis well over 5 μm on average (Figure 6a). Those made by glycine-nitrate combustion (Figure 6b) are greatly reduced in size and significantly shorter, although they still exhibit a large aspect ratio.

Lithium diffusion is highly anisotropic in these materials. A transmission electron microscopy (TEM) study on $Na_{0.44}MnO_2$ show that the tunnels are aligned parallel to the long axis of the needles.[1] Thus, reduction of the particle size in this dimension can be expected to improve rate capability by decreasing the Li diffusion path-length. This accounts for the better performance at high current densities of the shorter particles produced by GNC combustion

compared to those made by solid-state synthesis for both Li_xMnO_2 and $Li_xTi_{0.11}Mn_{0.89}O_2$. The improvement at high rates is particularly notable for the latter case where the differences in particle sizes are particularly acute. Additionally, the poorer performance of SS-$Li_xTi_{0.11}Mn_{0.89}O_2$ compared to Li_xMnO_2 is probably also attributable in part to the much longer particle length of the former.

Figure 7 a and b shows the effect of changing the current density on the characteristics of Li/SS-Li_xMnO_2 and GNC-Li_xMnO_2 cells. At low current densities, the differences in the shapes of the discharge profiles for these two cathode materials are evident, particularly above 4V. Raising the current density to 0.9 mA/cm^2 results in a decrease in the delivered capacity for both materials, although it is more severe for SS-Li_xMnO_2. The decrease is almost completely attributable to the loss of the high voltage capacity for both materials. This strongly suggests that there are more severe diffusional limitations associated with these high voltage processes than for the lower voltage ones.

In order to investigate this theory, a galvanostatic intermittent titration technique (GITT) experiment[17] on a Li/Li_xMnO_2 cell was carried out (Figure 8). Although the porous nature of the electrode precludes an absolute determination of diffusion coefficients, it is possible to obtain relative values as a function of the open circuit potential (OCV). The redox chemistry of this compound involves both solid-solution regions (sloping voltage profile regions) and rapid charge ordering transitions (voltage plateaus) allowing meaningful comparison of relative diffusion coefficients as a function of state-of-charge. The charge-ordering phase transitions below 4V are correlated with local minima in the log D vs. OCV plot. The diffusion coefficient, however, decreases most dramatically when the cell potential is raised above 4V, indicating much lower mobility for Li ions in this range. These values are most likely associated with movement of Li in and out of the small tunnels in the structure (Figure 1) whereas the lower voltage processes are associated with the larger tunnels. Similar

results were obtained on a Li/$Li_xTi_{0.11}Mn_{0.89}O_2$ cell, although the variation of log D with state-of-charge below 4V is less distinct than for the Li/Li_xMnO_2 case, because of the attenuation of the phase transitions induced by the Ti substitution.

The effect of partial titanium substitution on layered[18, 19, 20] or spinel[21] cathode materials has been previously studied. Except at very low levels, replacement of some electroactive Ni^{3+}, Co^{3+}, or Mn^{3+} ions with Ti^{4+} (and the resulting charge compensation involving other ions) results in somewhat decreased practical capacities, although other properties, such as rate capability, cycle life, and thermal stability may be improved. This is not surprising because the Ti^{3+}/Ti^{4+} redox couple in these types of structures is not active in the potential range generally employed. As was previously discussed, this may not be true for electrodes with the $Na_{0.44}MnO_2$ structure. It has also been suggested, however, that poorer electronic transport properties in some Ti-substituted compounds may be responsible for any observed decreases in capacities.[21] AC conductivity measurements on pressed pellets of SS-Li_xMnO_2 and SS-$Li_xTi_{0.11}Mn_{0.89}O_2$ (Figure 9) does indeed indicate that the latter is more electrically resistive than the latter by about half an order of magnitude or so. Both materials have somewhat lower conductivities than the parent compound $Na_{0.44}MnO_2$[22] but are within a similar range as other Mn^{3+}/Mn^{4+} oxides. Thus, it is likely that the electrochemical performances of both materials will depend somewhat on electrode fabrication details (e.g., amount of added carbon, thicknesses, etc.) as well as cell configuration, with $Li_xTi_{0.11}Mn_{0.89}O_2$ somewhat more sensitive to these effects than Li_xMnO_2.

The thermal characteristics of $Li_xTi_{0.11}Mn_{0.89}O_2$ also differ from those of Li_xMnO_2 significantly. Figure 10 shows DSC data on SS-Li_xMnO_2 and SS-$Li_xTi_{0.11}Mn_{0.89}O_2$ charged to 4.4 V (i.e., delithiated). The profile of SS-Li_xMnO_2 charged to 4.4V has two sharp exothermic peaks at about 130°C and 230°C. This relatively poor thermal abuse tolerance has negative safety implications for lithium batteries. In contrast, the exothermic transitions for

SS-$Li_xTi_{0.11}Mn_{0.89}O_2$ charged to 4.4V are smaller and occur at much higher temperatures (320°C and 335°C).

The better thermal abuse tolerance indicated by these results, and the improved dissolution resistance noted in the other studies cited previously, make titanium-substituted electrodes with the $Na_{0.44}MnO_2$ structure much more attractive for use in lithium battery configurations than Li_xMnO_2, in spite of the somewhat inferior electrochemical properties. The new results obtained in this study strongly imply that these can, however, be improved substantially. For example, synthesis techniques that result in shorter or more spherical particles should increase rate capabilities further. Optimization of electrode and cell fabrication to minimize impedances and the use of electrolytes with better oxidative stability (such as RTILs) should also improve utilization throughout a range of current densities.

Conclusions

Differences in the electrochemical properties of $Li_xTi_{0.11}Mn_{0.89}O_2$ electrodes compared to Li_xMnO_2 are attributable, in part, to changes in the voltage profiles induced by the Ti-substitution. Synthesis method also affects these profiles, as well as the particle sizes and morphologies. The latter strongly impacts the rate performance of the electrode materials, so that the poorest performing material at low current densities (GNC-$Li_xTi_{0.11}Mn_{0.89}O_2$) shows the best high-rate performance. Ti-substitution lowers the electronic conductivity, but results in greatly improved thermal stability, making it attractive for use in lithium batteries.

Acknowledgments

This work was supported by the Assistant Secretary for Energy Efficiency and Renewable Energy, Office of Vehicle Technologies of the U.S. Department of Energy under Contract No. DE-AC02-05CH11231.

References

1. Doeff, M. M.; Anapolsky, A.; Edman, L.; Richardson, T. J.; De Jonghe, L. C. *J. Electrochem. Soc*. **2001** *148,* 230.

2 . Armstrong, A. R.; Huang, H.; Jennings, R. A.; Bruce, P. G., *J. Mater. Chem*. **1998** *8,* 194.

3. Richardson T. J.; Ross, P. N., *The Electrochemical Society Meeting Abstracts*, Abstract 130 **1998** *98-2* Boston**,** MA**.**

4. Doeff, M. M.; Richardson, T. J.; Kepley, L. *J. Electrochem. Soc*. **1996** *143*, 2507.

5. Park, Y. J.;. Doeff, M. M *J. Power Sources* **2007** *165*, 573.

6. Doeff, M. M.; Richardson T. J.; Hwang K. T. *J. Power Sources* **2004** *135*, 240.

7. Akimoto, J.; Awaka, J.; Takahashi Y.; Kijama, N.; Tabuchi M.; Nakashima A.; Sakaebe H.; Tatsumi K., *Electrochem. Solid State Lett.* **2005** *8,* A554.

8. Saint, J. A.; Best, A.; Hollenkamp, A; Kerr J.; Shin, J.H.; Doeff, M. M. *J. Electrochem. Soc.*, in press.

9. Awaka, J. ; Akimoto, J. ; Hayakawa, H. ; Takahashi, Y. ; Kijima, N. ; Tabuchi, M. ; Sakaebe, H. ; Tatsumi, K. *J. Power Sources* **2007** *174,* 1218.

10. Jung, C. H.; Park, J. Y.; Oh, S. J.; Park, H. K.; Kim, Y.S.; Kim, D. K.; Kim, J. H. *J. Nucl. Mat.* **1998** *253*, 203.

11. Mumme, W.G. *Acta Crystallogr.* **1968** *B24*, 1114.

12. Doeff, M. M.; Peng, M.Y.; Ma, Y.; De Jonghe, L.C. *J. Electrochem. Soc.* **1994** *141*, L145.

13. Sauvage, F.; Laffont, L.; Tarascon, J.-M.; Baudrin, E. *Inorg. Chem.* **2007** *46*, 3289.

14. Thackeray, M. M. *J. Electrochem. Soc.* **1995** *142*, 2558.

15. Huang, S. Y.; Kavan, L.; Exnar, I.; Grätzel, M. *J. Electrochem. Soc.* **1995** *142*, L142.

16. Doeff, M. M.; Ding, L.; De Jonghe, L. C. *Mat. Res. Soc. Proc.* **1995** *393,* 107.

17. Wen, C. J.; Boukamp, B.A.; Huggins, R.A. *J. Electrochem. Soc.* **1979** *126*, 2258.

18. Kim J.; Amine K. *Electrochem. Comm.* **2001** *3,* 52.

19. Ganesan, M.; Sundararajan, S.; Dhananjeyan, M. V. T.; Sarangapani, K. B.; Renganathan, N. G. *Mat. Science and Eng. B* **2006** *131*, 203.

20. Ha, H. W.; Jeong, K. H.; Kim, *J. Power Sources* **2006** *161,* 606.

21. Kim, J. H.; Myung, S. T.; Yoon, C. S.; Oh, I. H.; Sun, Y. K. *J. Electrochem. Soc.* **2004** *151*, A1911.

22. Parant, J.-P.; Olazcuaga, R.; Devalette, M.; Fouassier, C.; Hagenmuller, P. *J. Sol. State Chem.* **1971** *3*, 1.

Table 1. Cell Potentials of Main Peaks in the dQ/dV plots of Li/Li_xMnO_2 and $Li/Li_xTi_{0.11}Mn_{0.89}O_2$ cells (Figure 2).

Electrode	Li_xMnO_2		$Li_xTi_{0.11}Mn_{0.89}O_2$	
Preparation method	S.S.	GNC	S.S.	GNC
	Ch./Disch.	Ch./Disch.	Ch./Disch.	Ch./Disch.
Peak positions (V)[a]				4.53/4.51
		4.52, 4.40/4.35	/4.38	/4.38
	4.23/4.19	4.23/4.16	4.28/4.16	
	3.36/3.30, 3.25	3.35/3.31	3.38/3.34, 3.23	3.36/3.31
		3.17/3.11		
	3.20/3.08, 3.11	3.09/3.04	3.19, 3.13/3.07	3.19, 3.08/3.03

Figure Captions

Figure 1. Structure of $Na_{0.44}MnO_2$. MnO_6 octahedra (yellow) and MnO_5 square pyramids (gray) link together to form tunnels in which sodium ions (black spheres) are located.

Figure 2. (a) Indexed XRD powder pattern of SS-$Na_{0.44}MnO_2$; observed (—), calculated (···), difference (—) and (b) powder patterns, from top to bottom, of SS-$Na_{0.44}MnO_2$, SS-Li_xMnO_2, SS-$Na_{0.44}Ti_{0.11}Mn_{0.89}O_2$ and SS-$Li_xTi_{0.11}Mn_{0.89}O_2$.

Figure 3. Results of potentiostatic experiments on Li/1M $LiPF_6$, EC-DMC/Li_xMnO_2 or $Li_xTi_{0.11}Mn_{0.89}O_2$ cells (a) SS-Li_xMnO_2, (b) GNC-Li_xMnO_2, (c) SS-$Li_xTi_{0.11}Mn_{0.89}O_2$ and (d) GNC-$Li_xTi_{0.11}Mn_{0.89}O_2$. Cells were stepped in 10 mV increments between 4.8-2.5V at approximately C/100 rate. dQ/dV plots are shown for the first three cycles (dashed line=first cycle) and the voltage profile is shown for the first discharge, obtained by integrating the dQ/dV data.

Figure 4. Modified Peukert plot showing the rate capabilities of Li/Li_xMnO_2 and $Li_xTi_{0.11}Mn_{0.89}O_2$ cells.

Figure 5. Scanning electron micrographs of (a) SS-$Na_{0.44}MnO_2$ powder and (b) GNC-$Na_{0.44}MnO_2$ powder.

Figure 6. Scanning electron micrographs of (a) SS-$Na_{0.44}Ti_{0.11}Mn_{0.89}O_2$ powder and (b) GNC-$Na_{0.44}Ti_{0.11}Mn_{0.89}O_2$ powder.

Figure 7. Discharge profiles of Li/SS-Li_xMnO_2 and GNC-Li_xMnO_2 cells charged and discharged at (a) 0.033 mA/cm^2 (~C/33 rate) and (b) 0.9 mA/cm^2 (~0.75 C rate).

Figure 8. Relative diffusion coefficients as a function of the open circuit potential of a Li/SS-Li_xMnO_2 cell subjected to a galvanostatic intermittent titration technique experiment (inset) between 4.4 and 2.5V. The cell was charged or discharged at a current density of 0.075 mA/cm^2 for 0.675h and allowed to rest for three hours before the next increment of charge was passed. Data points were taken from the second charge (initial partial charge not shown).

Figure 9. Arrhenius plots of the ac conductivities of SS-Li_xMnO_2 and SS-$Li_xTi_{0.11}Mn_{0.89}O_2$ pressed pellets.

Figure 10. Differential scanning calorimetry profiles (10°C.min^{-1}) of SS-Li_xMnO_2 and SS-$Li_xTi_{0.11}Mn_{0.89}O_2$ charged to 4.4V.

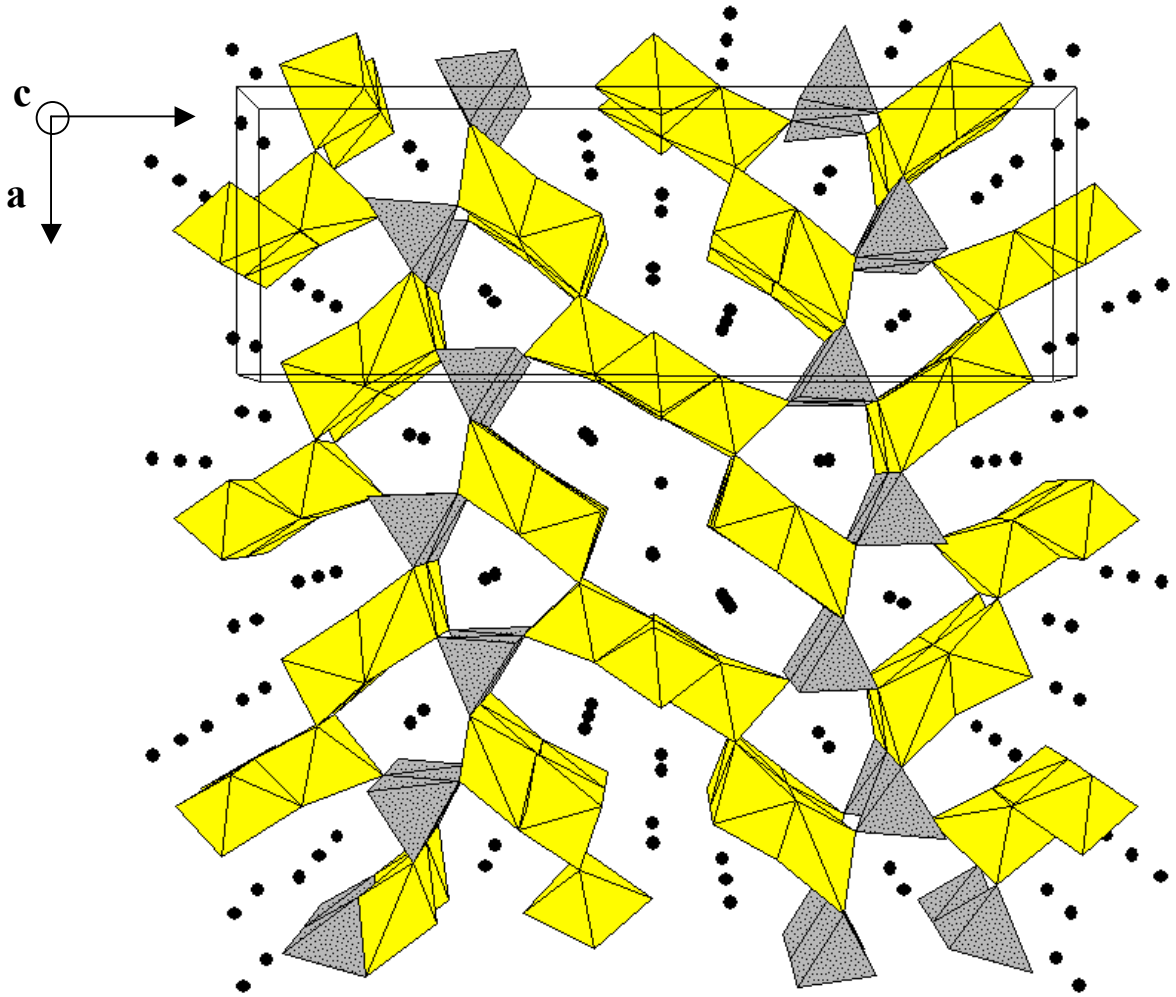
c
a

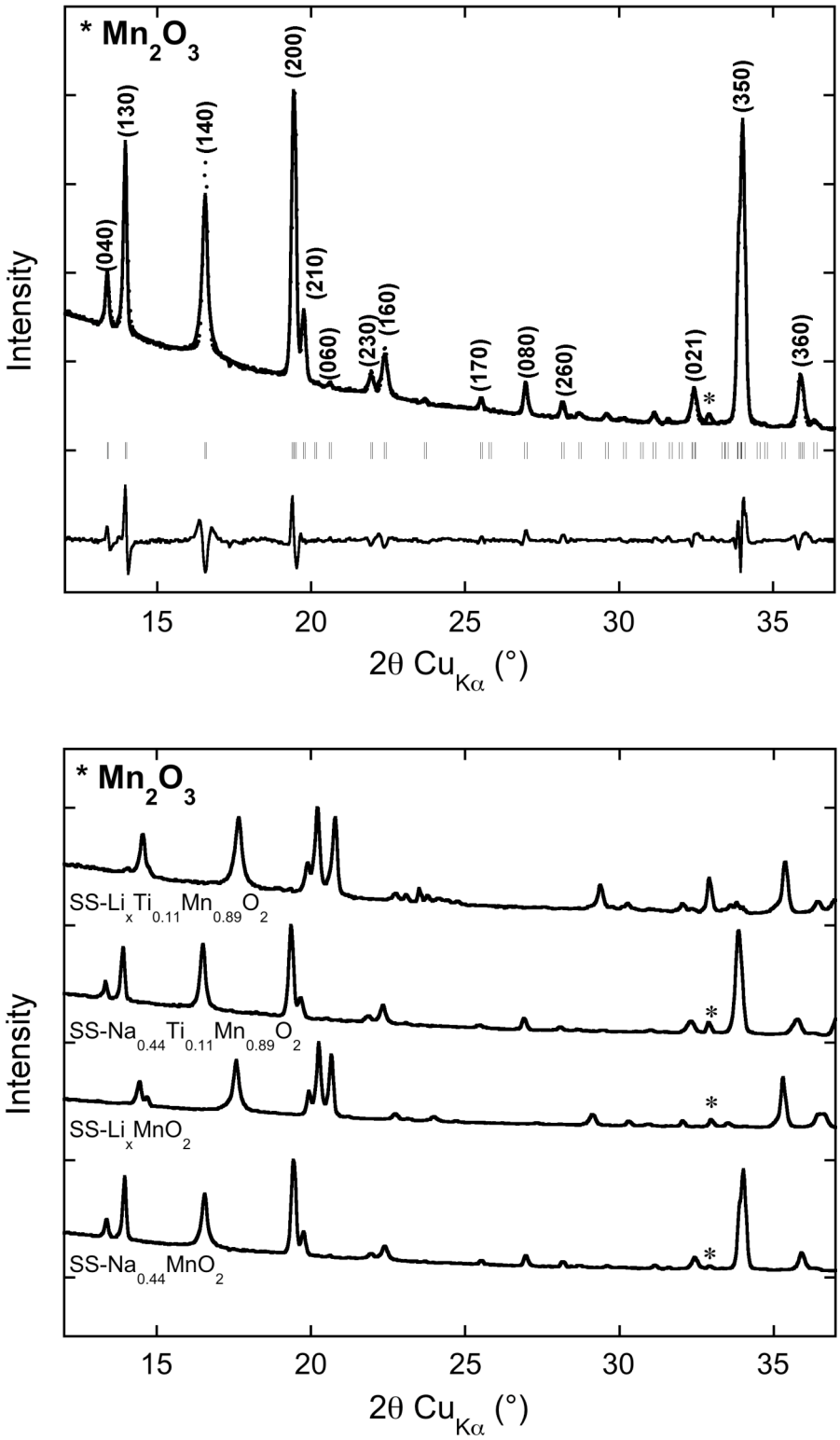
* Mn2O3
(040)
(130)
(140)
(200)
(210)
(060)
(230)
(160)
(170)
(080)
(260)
(021)
(350)
(360)
Intensity
15
20
25
30
35
2θ Cu Kα (°)
(a)
* Mn2O3
SS-Lix Ti0.11 Mn0.89 O2
SS-Na0.44 Ti0.11 Mn0.89 O2
SS-Lix MnO2
SS-Na0.44 MnO2
Intensity
15
20
25
30
35
2θ Cu Kα (°)
(b)

Figure 2

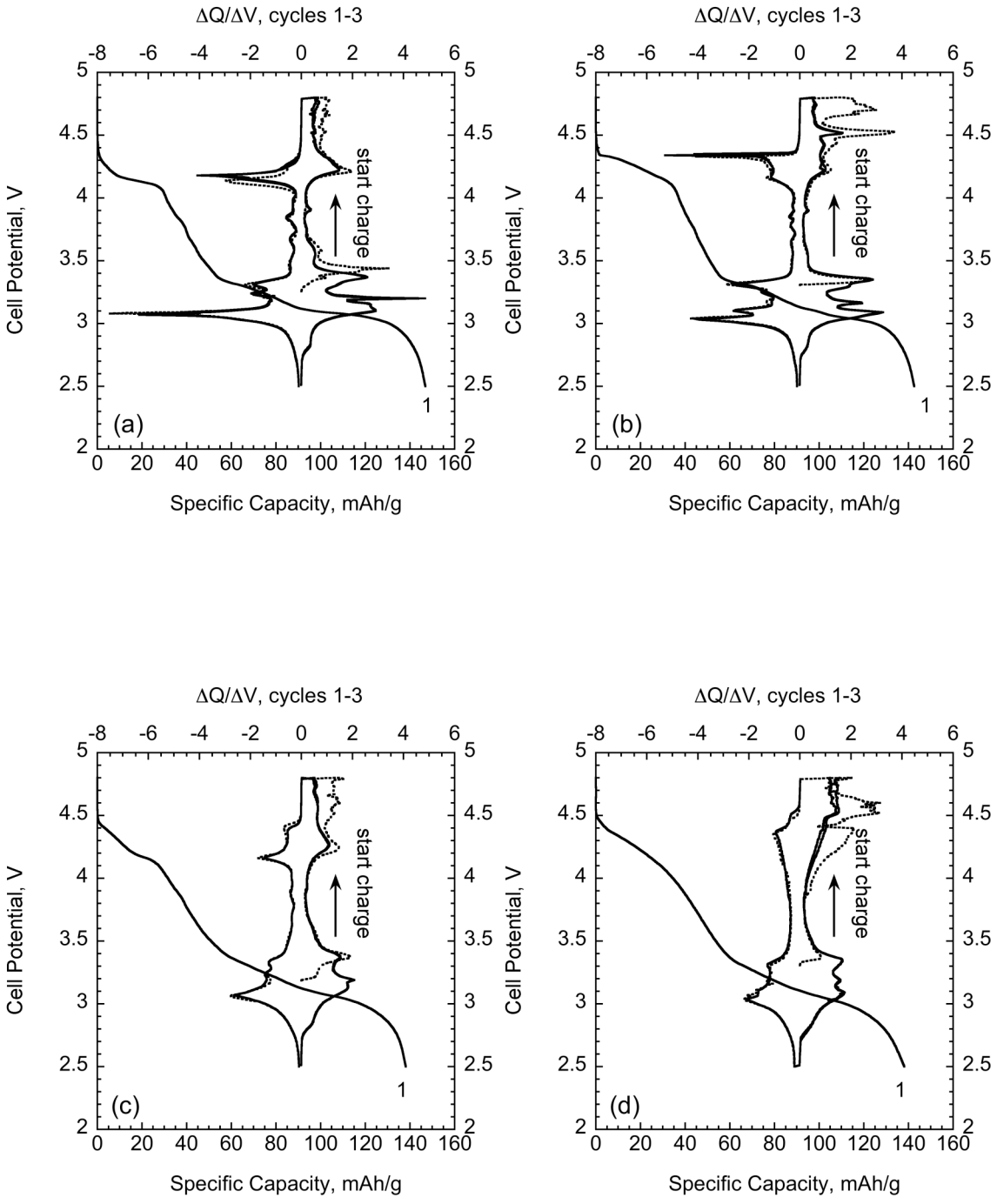
ΔQ/ΔV, cycles 1-3
Cell Potential, V
Specific Capacity, mAh/g
start charge
1
(a)
(b)
(c)
(d)

Figure 3

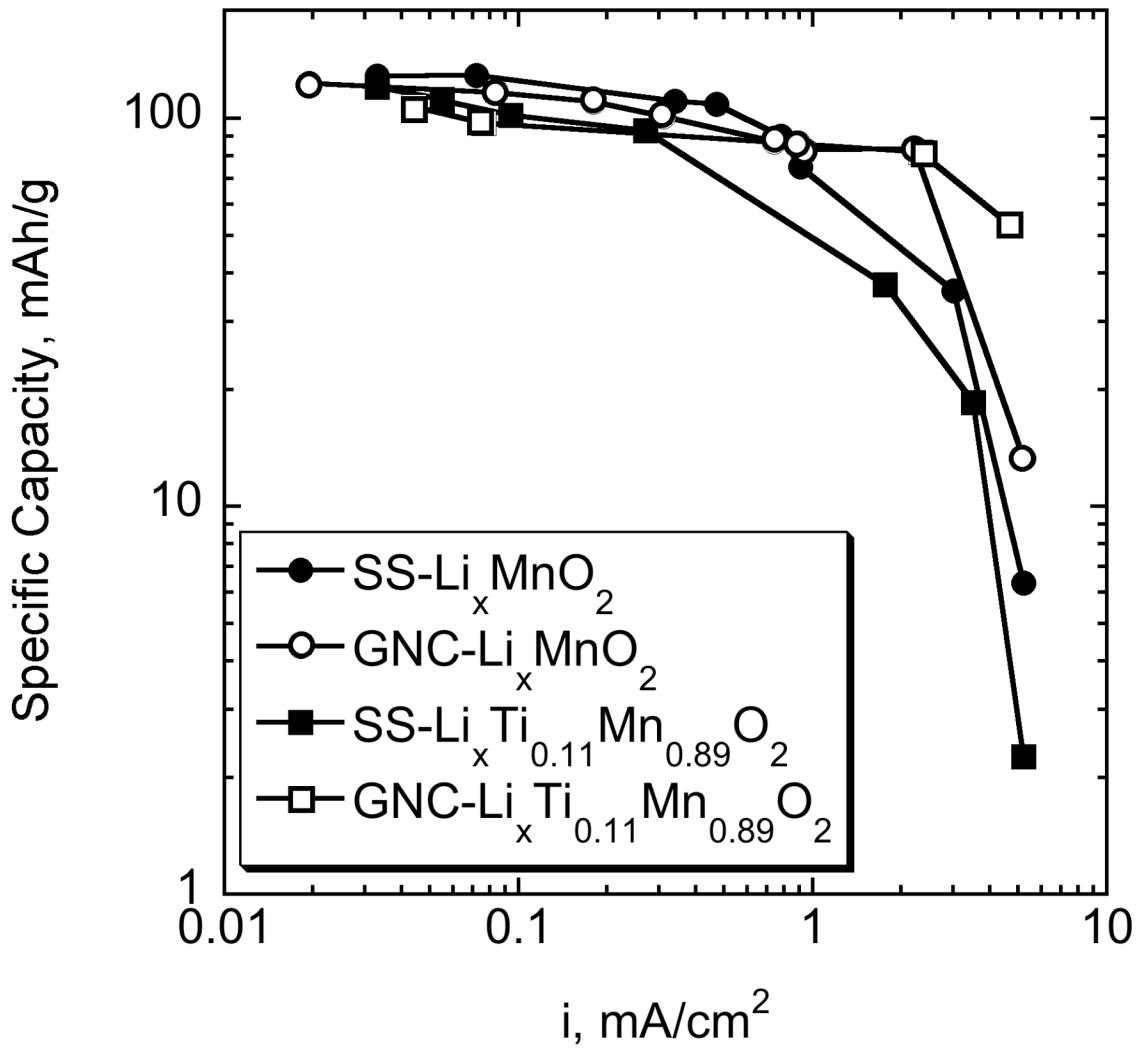
Specific Capacity, mAh/g
100
10
1
0.01
0.1
1
10
i, mA/cm2
SS-LixMnO2
GNC-LixMnO2
SS-LixTi0.11Mn0.89O2
GNC-LixTi0.11Mn0.89O2

Figure 4

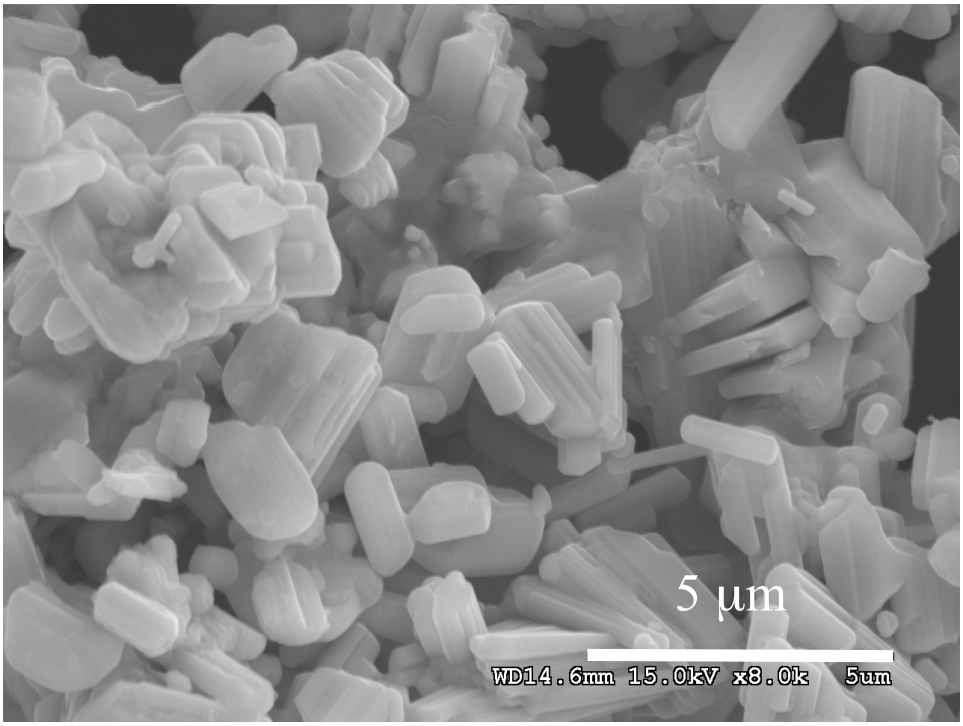

(a)

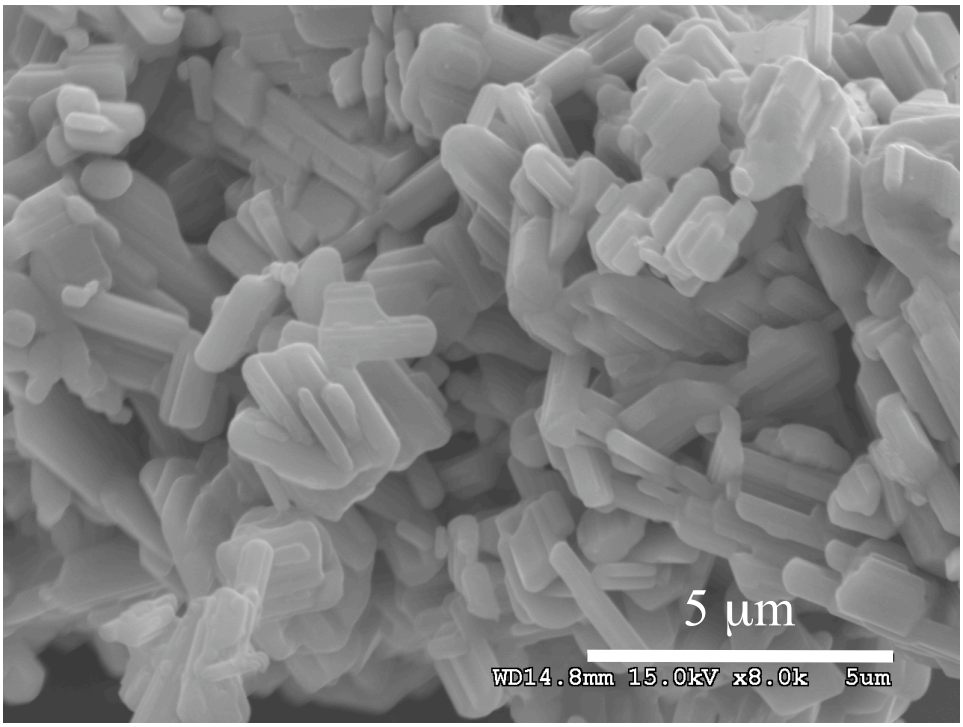

(b)

Figure 5

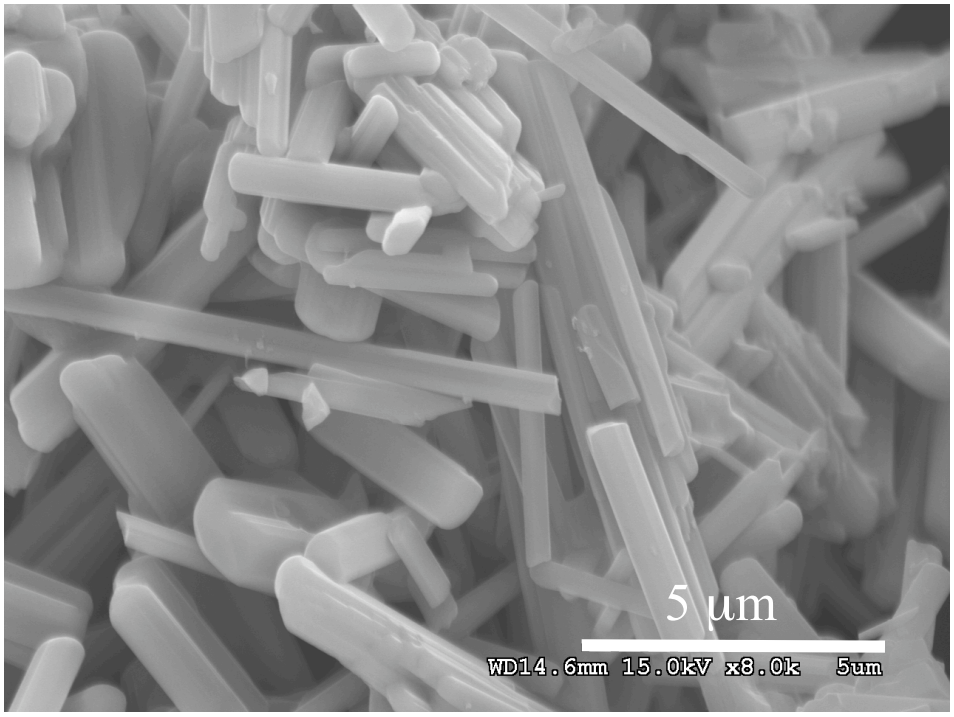

(a)

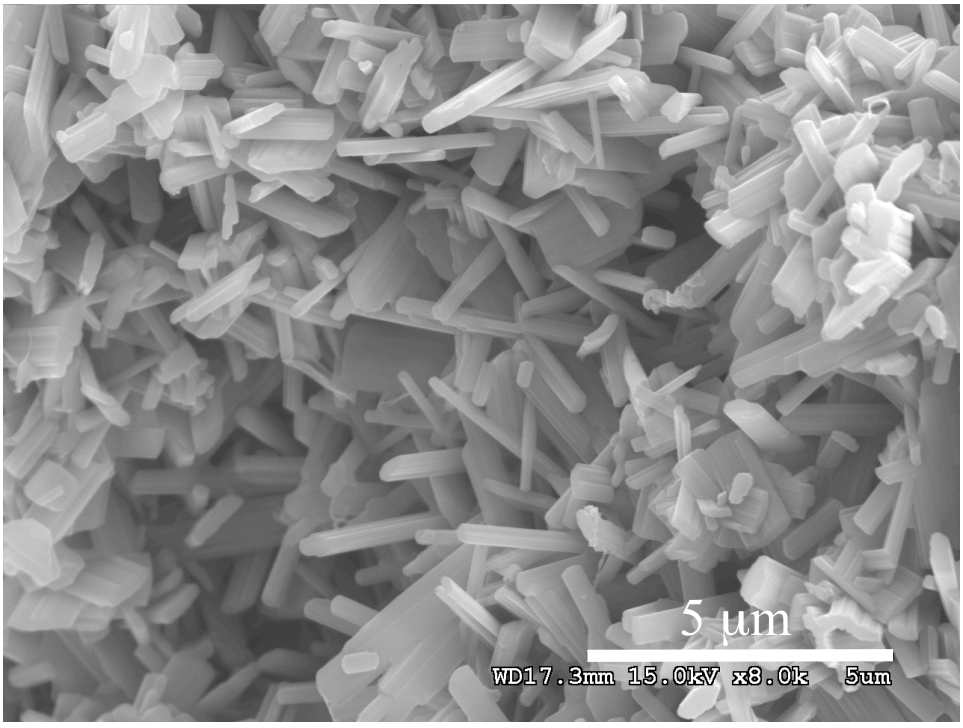

(b)

Figure 6

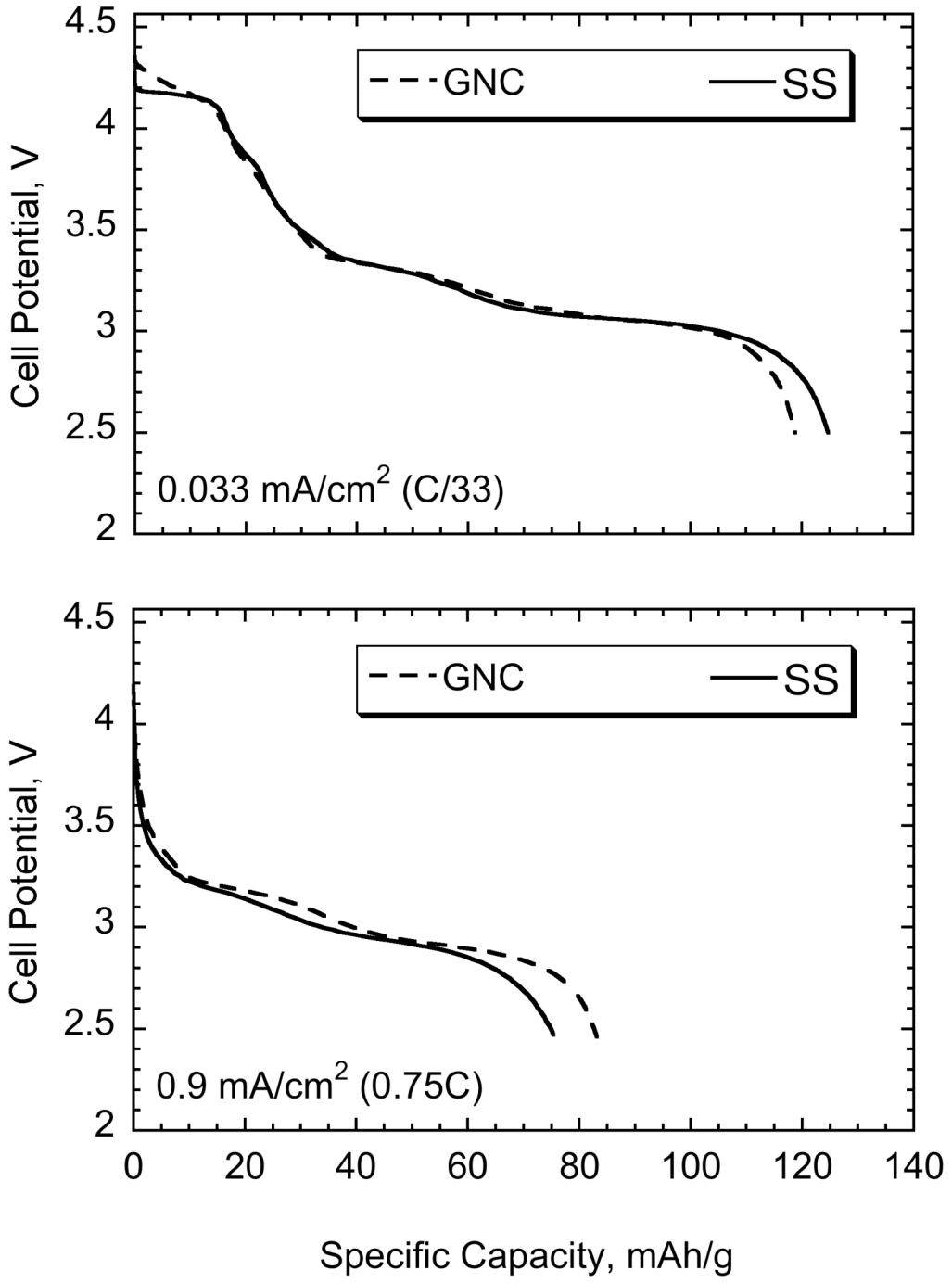
4.5
4
3.5
3
2.5
2
Cell Potential, V
GNC
SS
0.033 mA/cm2 (C/33)
(a)
4.5
4
3.5
3
2.5
2
Cell Potential, V
GNC
SS
0.9 mA/cm2 (0.75C)
(b)
0
20
40
60
80
100
120
140
Specific Capacity, mAh/g

Figure 7

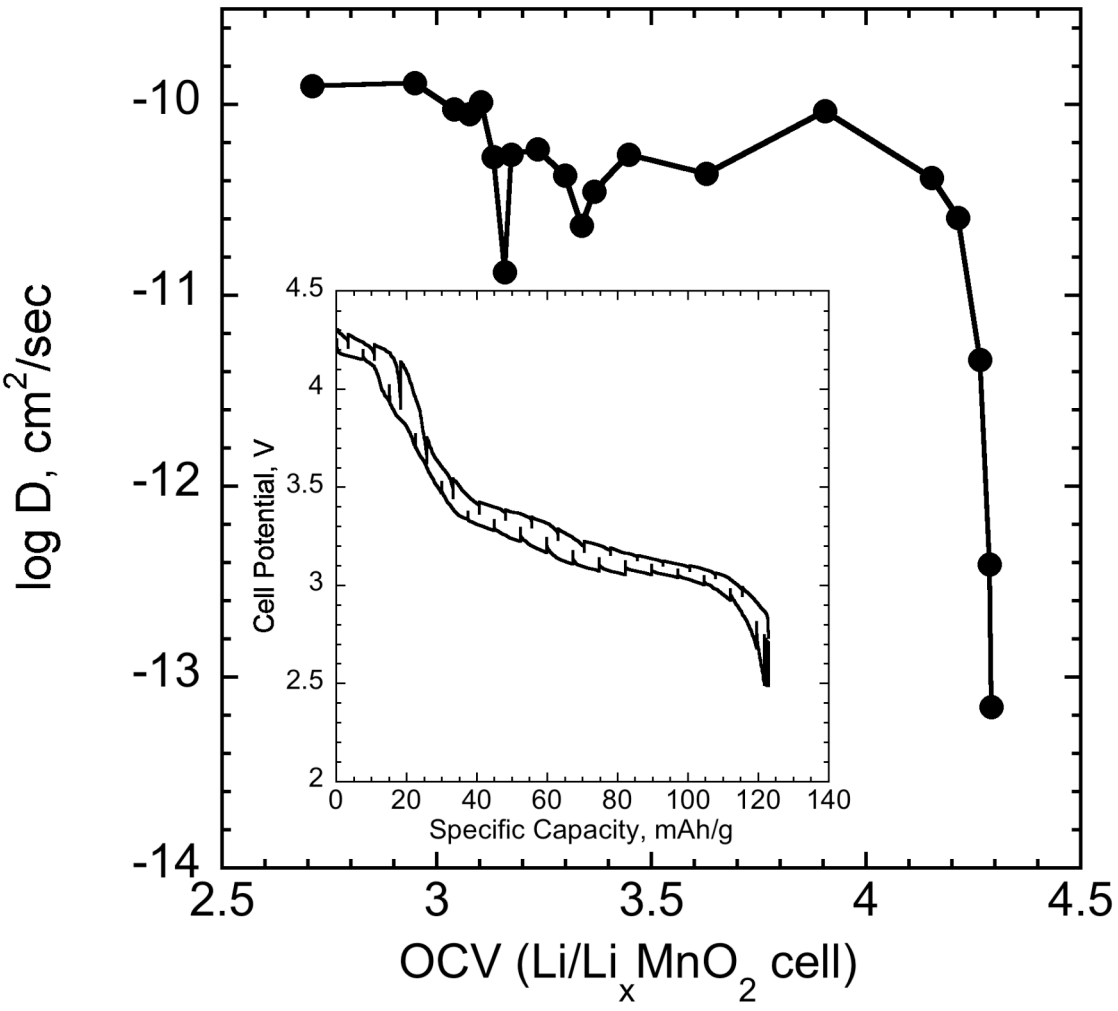
log D, cm²/sec
-10
-11
-12
-13
-14
2.5
3
3.5
4
4.5
OCV (Li/Li$_x$MnO$_2$ cell)
Cell Potential, V
4.5
4
3.5
3
2.5
2
0
20
40
60
80
100
120
140
Specific Capacity, mAh/g

Figure 8

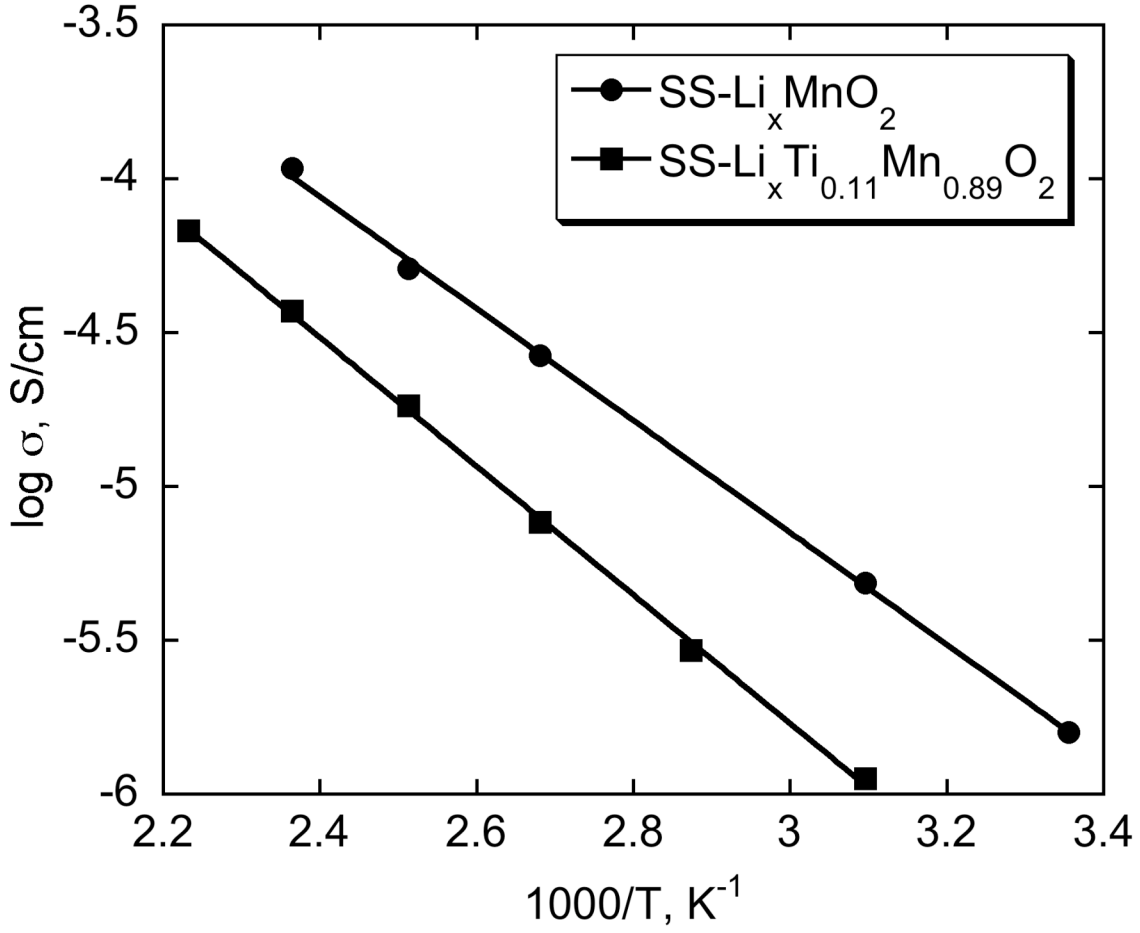
-3.5
-4
-4.5
-5
-5.5
-6
log σ, S/cm
2.2
2.4
2.6
2.8
3
3.2
3.4
1000/T, K-1
SS-LixMnO2
SS-LixTi0.11Mn0.89O2

Figure 9

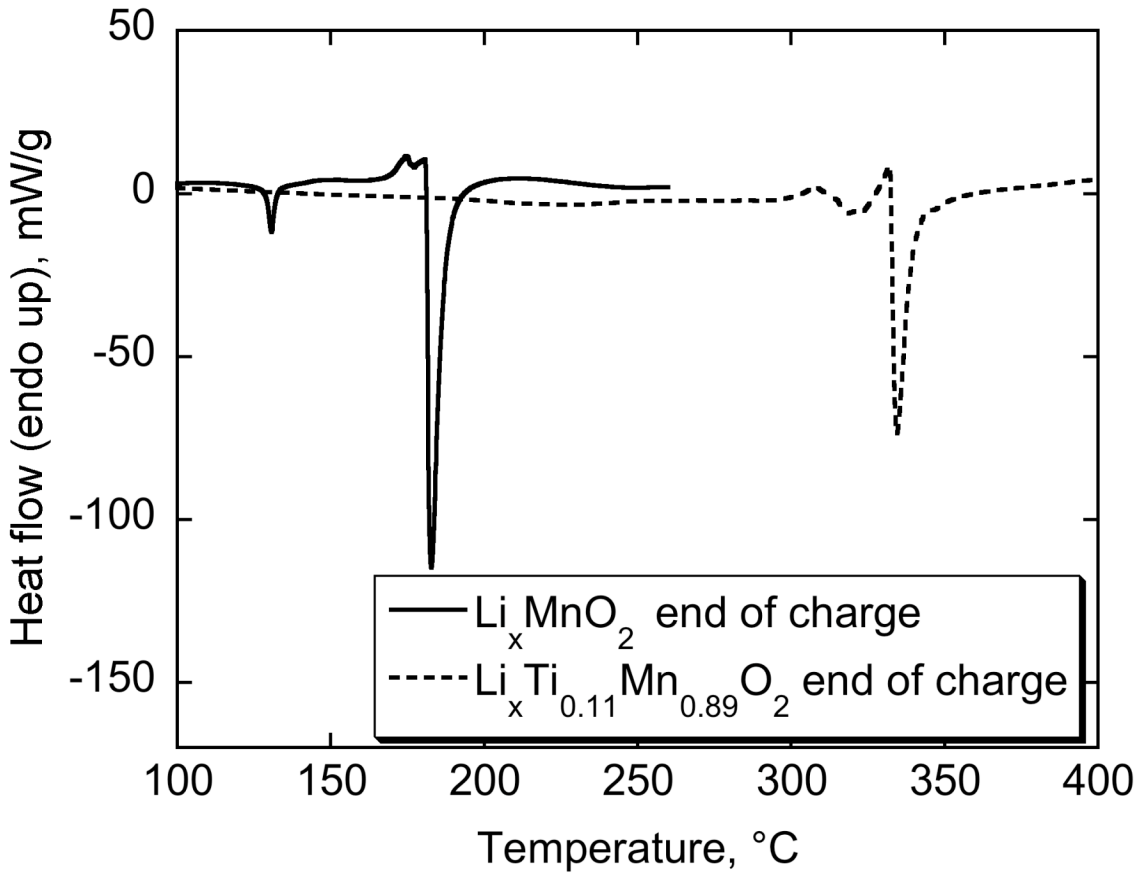
50
0
-50
-100
-150
Heat flow (endo up), mW/g
100
150
200
250
300
350
400
Temperature, °C
Li$_x$MnO$_2$ end of charge
Li$_x$Ti$_{0.11}$Mn$_{0.89}$O$_2$ end of charge

Figure 10